Journal of Energy Chemistry 55 (2021) 10–16

Contents lists available at ScienceDirect

Journal of Energy Chemistry

journal homepage: www.elsevier.com/locate/jechem

http://www.journals.elsevier.com/journal-of-energy-chemistry/

In-situ surface self-reconstruction in ternary transition metal dichalcogenide nanorod arrays enables efficient electrocatalytic oxygen evolution

Qiang Chen [a,b], Yulu Fu [a,b], Jialun Jin [a], Wenjie Zang [b], Xiong Liu [a], Xiangyong Zhang [b], Wenzhong Huang [a], Zongkui Kou [b,*], John Wang [b], Liang Zhou [a,c,*], Liqiang Mai [a,c,*]

[a] State Key Laboratory of Advanced Technology for Materials Synthesis and Processing, Wuhan University of Technology, Wuhan 430070, Hubei, China
[b] Department of Materials Science and Engineering, National University of Singapore, Singapore 117574, Singapore
[c] Foshan Xianhu Laboratory, Foshan 528216, Guangdong, China

ARTICLE INFO

Article history:
Received 23 May 2020
Revised 30 June 2020
Accepted 1 July 2020
Available online 9 July 2020

Keywords:
Surface self-reconstruction
Transition metal dichalcogenide
Transition metal oxyhydroxide
Oxygen evolution reaction
Water splitting

ABSTRACT

Water splitting has received more and more attention because of its huge potential to generate clean and renewable energy. The highly active and durable oxygen evolution reaction (OER) catalysts play a decisive factor in achieving efficient water splitting. The identification of authentic active origin under the service conditions can prompt a more reasonable design of catalysts together with well-confined micro-/nano-structures to boost the efficiency of water splitting. Herein, Fe, Co, and Ni ternary transition metal dichalcogenide (FCND) nanorod arrays on Ni foam are purposely designed as an active and stable low-cost OER pre-catalyst for the electrolysis of water in alkaline media. The optimized FCND catalyst demonstrated a lower overpotential than the binary and unary counterparts, and a 27-fold rise in kinetic current density at the overpotential of 300 mV compared to the nickel dichalcogenide counterpart. Raman spectra and other structural characterizations at different potentials reveal that the *in-situ* surface self-reconstruction from FCND to ternary transition metal oxyhydroxides (FCNOH) on catalyst surfaces initiated at about 1.5 V, which is identified as the origin of OER activity. The surface self-reconstruction towards FCNOH also enables excellent stability, without fading upon the test for 50 h.

1. Introduction

Electrochemical water splitting is a promising solution that can achieve large-scale hydrogen production to meet the ever-rising demand for sustainable energy and clean environment [1–3]. For efficient oxygen evolution reaction (OER) at the anode, it is essential to develop highly efficient and economical electrocatalysts [4–6]. Nevertheless, most of the known OER electrocatalysts are suffering from the poor reaction kinetics associated with multiple proton-electron transfer reaction [7,8]. Therefore, it remains a haunting challenge to significantly reduce the large overpotential and accelerate the OER kinetics of the catalysts [9–11]. Transition metal (TM)-based materials, especially nickel-based, as a class of potential substitutes for the precious metal catalysts, have attracted considerable attention in recent years, which can be attributed to their unique electronic structures making them suitable for binding with oxygen-involving intermediates [12–14]. Among the most active Ni-based OER catalysts [12,15–17], nickel sulfides (such as NiS [18,19], NiS_2 [20,21], and Ni_3S_2 [22–24]) have been widely explored, where nickel dichalcogenide (ND) phase is notable for its metal-like properties [25–28]. For example, Feng *et al.* devised high-index faceted Ni_3S_2 nanosheets formed on nickel foam (NF), which exhibited excellent OER electrocatalytic activity [29]. Nevertheless, the ND materials in general forms cannot afford enough active sites for OER [30]. In order to boost the intrinsic performance of ND, the introduction of additional earth-abundant metals and micro-/nano-structure engineering have been widely explored as effective strategies, where they can optimize the adsorption/desorption strength of OER intermediates and exposes more active sites on surfaces under service conditions by the synergy of multielement, enriched high-valence species, and good

* Corresponding authors at: State Key Laboratory of Advanced Technology for Materials Synthesis and Processing, Wuhan University of Technology, Wuhan 430070, Hubei, China (L. Zhou, L. Mai). Department of Materials Science and Engineering, National University of Singapore, Singapore 117574, Singapore (Z. Kou).

E-mail addresses: msekz@nus.edu.sg (Z. Kou), liangzhou@whut.edu.cn (L. Zhou), mlq518@whut.edu.cn (L. Mai).

https://doi.org/10.1016/j.jechem.2020.07.005

structural stability [30–36]. Therefore, it is necessary to purposely design a proper polynary transition metal dichalcogenide to enhance the catalytic activity.

In addition to increasing the intrinsic active sites by the rational construction of polynary transition metal dichalcogenide and micro-/nano-structure engineering, it would be equally necessary to identify their active origin on the catalyst surface for further optimization of catalysts [37–39]. For most of the TM X-ide-based electrocatalysts (X-ides are sulfides, phosphides, carbides, nitrides, and oxides), they are actually OER pre-catalysts, not the "real" catalysts, because their composition, phase, and morphology will undergo a dramatic change during the OER process, especially in strong alkaline environments [40–43]. For example, Zou and his co-workers found that nickel–iron dichalcogenide self-reconstructs their surfaces during OER by *ex-situ* characterizations, giving rise to a steady growth of the self-assembled metal–oxygen (hydroxide) active layers [44]. Although previous studies have accumulated some of the knowledge on accelerating OER kinetics by surface/subsurface self-reconstruction, it would make a lot of sense to fully understand the surface phase evolution, by conducting structural and surficial studies in the serving conditions, and trace the actual active origin(s) in the dynamic process, for the rational design of OER catalysts/pre-catalysts.

Herein, we purposely design the Fe-Co-Ni ternary transition metal dichalcogenide (FCND) nanorod arrays on NF by a one-step hydrothermal process, aiming at improving the intrinsic OER kinetics and overall performance. The FCND thus-prepared exhibits outstanding OER catalytic activity with remarkably decreased overpotential and Tafel slope in 1.0 M KOH compared with its binary and unary counterparts, together with excellent long-term durability for OER (almost no activity fading after 50 h). Potential-dependent Raman spectra, X-ray diffraction (XRD), and transmission electron microscopy (TEM) reveal that the FCND actually functions as a pre-catalyst in the alkaline OER environment, and there is a steady surface reconstruction initialized at ~1.5 V to ultrathin ternary transition metal oxyhydroxides (FCNOH) shells formed *in-situ* on the FCND surfaces, which is largely responsible for the fast and stable OER kinetics.

2. Results and discussion

2.1. Synthesis and characterizations of FCND

The fabrication process for the FCND is schematically shown in Fig. 1(a). Due to the strong etching ability of Na_2S, the FCND was synthesized via a one-step hydrothermal process on NF in a solution containing Na_2S, $FeSO_4{\cdot}7H_2O$, $Co(NO_3)_2{\cdot}6H_2O$, urea, $Na_3C_6H_5O_7{\cdot}2H_2O$ without any additional nickel source.

To study the formation mechanism of the FCND nanorod arrays, contrast experiments are conducted, where the materials as-derived are termed as nickel dichalcogenide (ND), iron/nickel dichalcogenide (FND), and cobalt/nickel dichalcogenide (CND), respectively. The scanning electron microscopy (SEM) image of the ND is shown in Fig. 1(b), which shows the ND nanoparticles are uniformly grown on the three-dimensional network structure of NF. SEM images (Fig. S1a–c, supporting information) of the CND exhibit a nanorod structure with 3–4 μm in length, suggesting that the introduction of Co affected the morphology evolution of the nanorods. The morphology of FND showed uneven nanosheets on NF (Fig. S1d–f), which indeed indicated that unlike Co, Fe could induce the evolution of nanosheets. Interestingly, after both Fe and Co ions are introduced, the nanorod morphology of FCND can be easily observed in SEM (Fig. 1c), demonstrating that Fe and Co are working in a "role-playing" role for the formation of the hierarchical structure. The enlarged SEM image (Fig. 1d) further shows the FCND nanorods are of about 100–200 nm in diameter. Besides, compared with CND nanorods, the FCND nanorods are shorter and have a rougher surface. The morphology and structure of the FCND nanorods are further analyzed by using TEM. Fig. 1(e) shows the surface of the FCND with a length of about 400 nm. High-resolution TEM (HRTEM) image (Fig. 1f) reveals the lattice fringes of the nanorod, the clear lattice fringes of 0.41, 0.21, and 0.24 nm are observed and well-indexed to the (1 0 1), (2 0 2), and (0 0 3) planes of Ni_3S_2 (JCPDS no. 44-1418) [23], respectively. Moreover, the FCND nanorod is highly crystalline, as evidenced by the bright diffraction spots in the selected area electron diffraction (SAED) (Fig. 1g). The energy dispersive spectroscopy (EDS) elemental mapping (Fig. 1h) verifies the rather uniform existence of Fe, Co, Ni, and S. As observed, the signal of Fe, Co, and Ni are well-matched with the nanorod region, indicating that a ternary transition metal dichalcogenide composed of Fe, Co, and Ni are formed.

To investigate the phases in the products, we conduct further studies using XRD and Raman. Fig. 2(a) shows the XRD pattern of the FCND. Except for the three typical metallic Ni (JCPDS no. 04-0850) peaks [45], six characteristic diffraction peaks can be observed at 21.8°, 31.1°, 37.8°, 44.3°, 49.7°, and 55.2°, which can be indexed to the (1 0 1), (1 1 0), (0 0 3), (2 0 2), (1 1 3), and (1 2 2) planes of Ni_3S_2 (JCPDS no. 44-1418). Combining with the comparative investigation of XRD patterns (Fig. S2), the intensities of the ND diffraction peak prior to the introduction of Fe and Co was significantly weaker. The Raman spectrum (Figs. 2b and S3) reveals that the vibrational bands at 211, 250, 327, 346, and 372 cm^{-1} in the low wavenumber region are attributed to Ni_3S_2 [46,47], confirming that there was no phase change caused by introducing Fe and Co elements.

To determine the surface chemistry composition of sample, X-ray photoelectron spectroscopy (XPS) is conducted and compared with those of ND and FCND. Fig. S4 shows the XPS survey spectra of the as-prepared ND and FCND. Additional Fe and Co signals are observed for the FCND (Fig. S4), further confirming that Fe and Co are successfully introduced into Ni_3S_2. The Ni 2p XPS spectra are shown in Fig. 2(c) and S5. The ND and FCND show two main peaks located at 855.9 and 873.7 eV, which can be ascribed to Ni^{2+} [48]. Meanwhile, two extra peaks at 853.0 ($2p_{3/2}$) and 870.3 eV ($2p_{1/2}$) suggest a metallic state of Ni^0 [49]. Compared to ND, the FCND nanorod structure grows directly on the NF surface, such that some metallic Ni is exposed. However, the weak Co 2p and Fe 2p signals (Fig. 2d, e) are difficult to analyse because the Co 2p and Fe 2p signals overlap with the Ni signal [30]. Co 2p and Fe 2p in FCND show weak characteristic signals, which once again suggest the introduction of Fe and Co in Ni_3S_2. It can be seen from the weak Fe 2p signal in Fig. 2(e), the two peaks located at 710.7 and 722.4 eV can be ascribed to Fe^{3+}. The S 2p XPS spectra are shown in Fig. 2f and S6, the components located at 162.6 and 163.8 eV correspond to S $2p_{3/2}$ and S $2p_{1/2}$, which are typical characteristic peaks of S^{2-} coordinated with metal ions (M-S, M: Fe, Co, and Ni) [25]. The peaks at 168.5 and 170.0 eV are attributed to the presence of SO_4^{2-} in the samples [29], as they are partially oxidized during the vulcanization processes.

2.2. Electrochemical performance of OER electrocatalyst

The electrocatalytic performance of FCND toward OER in alkaline medium (1.0 M KOH) is evaluated using a typical three-electrode system. For comparison, we also study the performance of NF, unary ND, binary FND, and CND, as well as commercial IrO_2/C. Fig. 3(a) presents the polarization curves of all studied electrodes. The NF, ND, CND, FND, FCND, and IrO_2/C electrodes exhibit onset potentials of ~1.515, 1.539, 1.569, 1.529, 1.47, and 1.41 V vs. reversible hydrogen electrode (RHE), respectively (Fig. S7). To exclude the influence of the oxidation peak prior to OER on the

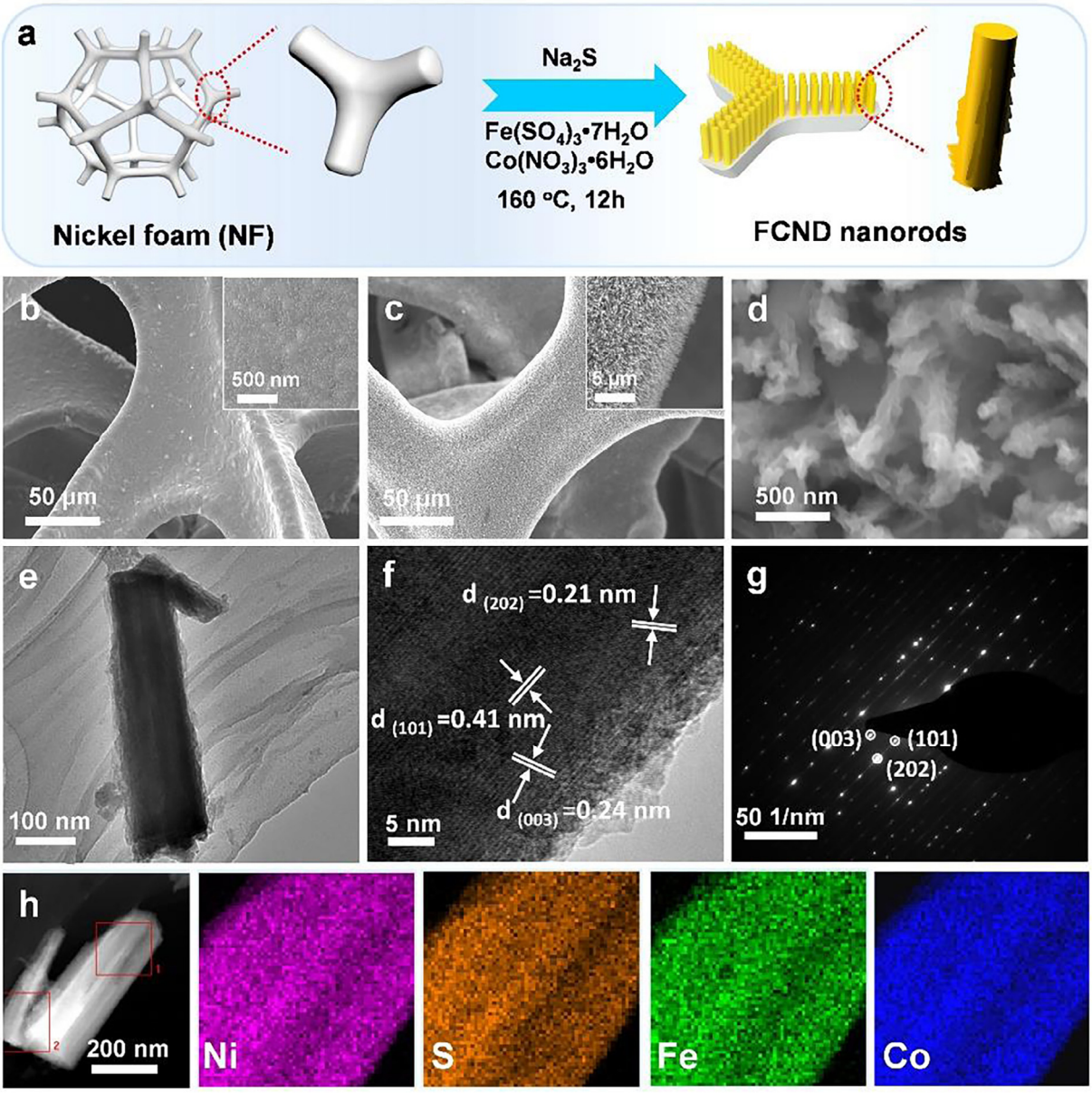

Fig. 1. Schematic of the synthesis process for free-standing FCND on NF (a). SEM images of the ND nanoparticles (b). SEM images of the as-prepared FCND nanorod array at different magnifications (c, d). TEM image (e), HRTEM image (f), and SAED pattern of the FCND nanorod (g). High-angle annular dark-field scanning transmission electron microscopy (HAADF-STEM) image of the FCND nanorod and corresponding element mapping images (h).

evaluation of OER performance, we extract the overpotentials at 50 mA cm^{-2}. The overpotential (η) of FCND is 337 mV at 50 mA cm^{-2} for OER, much lower than that of NF (499 mV), ND (426 mV), CND (471 mV), FND (380 mV) and IrO_2/C (>500 mV) at the same current density (Fig. 3b). Obviously, NF has a much lower intrinsic OER activity, while the activity of the free-standing Ni_3S_2 is increased. Interestingly, the introduction of Co can lower the OER activity, due to the decrease in electrochemical surface area, while the introduction of Fe significantly enhances the OER activity. When both Fe and Co are introduced, the FCND electrode shows excellent OER electrocatalytic performance, which is much better than that of most recently reported Ni-based electrocatalysts, including for example, Ni_3S_2/NF ($\eta_{\bar{1}0}^{-2}$ mA cm at 260 mV) [29], Ni_3S_2 ($\eta_{\bar{1}0}^{-2}$ mA cm at 340 mV) [50], NiS/NF ($\eta_{\bar{2}0}^{-2}$ mA cm at 320 mV) [51], Ni_{14}-$Cu_{55}P_1$ ($\eta_{\bar{1}0}^{-2}$ mA cm at 318.7 mV) [10], Fe-Ni_3S_2/FeNi ($\eta_{\bar{1}0}^{-2}$ mA cm at 282 mV) [52], $NiCo_2S_4$/NF ($\eta_{\bar{1}0}^{-2}$ mA cm at 260 mV) [53], $NiCo_2O_4$/NF ($\eta_{\bar{1}0}^{-2}$ mA cm at 330 mV) [53].

At low current densities, it can be affected by the oxidation peak of nickel-based materials. The overpotential at high current density is one of the most important indicators to evaluate OER activity. Specifically, the overpotential of the FCND electrodes at 20, 40, 60, 80, 100 mA cm^{-2} is 286.4, 322.2, 352.2, 381.1, and 408.4 mV, respectively (Fig. 3c), which are significantly lower than those of the contrast samples. The Tafel slopes are evaluated for catalytic reaction rates, as shown in Fig. 3(d). The FCND has a smaller Tafel slope value of 77 mV dec^{-1} than those of the contrast samples. This indicates that the FCND electrocatalysts endow with favorable OER kinetics.

To further understand the enhanced OER activity of FCND, the effective electrochemical active surface area (ECSA) of the electrodes is calculated by measuring the double-layer capacitance (C_{dl}) from the CV results at different scan rates (Fig. S8). The relationship curve between the measured current density and the scan rate is shown in Fig. 3(e) and the calculated capacitances of ND and

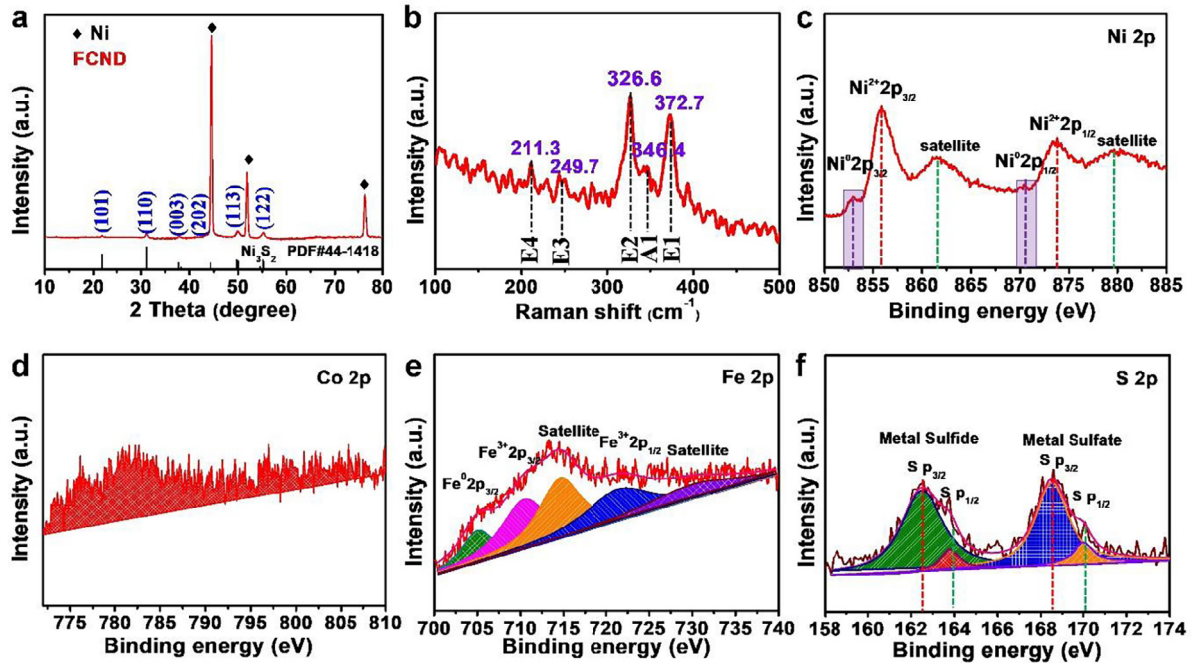

Fig. 2. Structure characteristics of the FCND. XRD pattern (a), Raman spectrum (b), and XPS spectra of Ni 2*p* (c), Co 2*p* (d), Fe 2*p* (e), and S 2*p* (f).

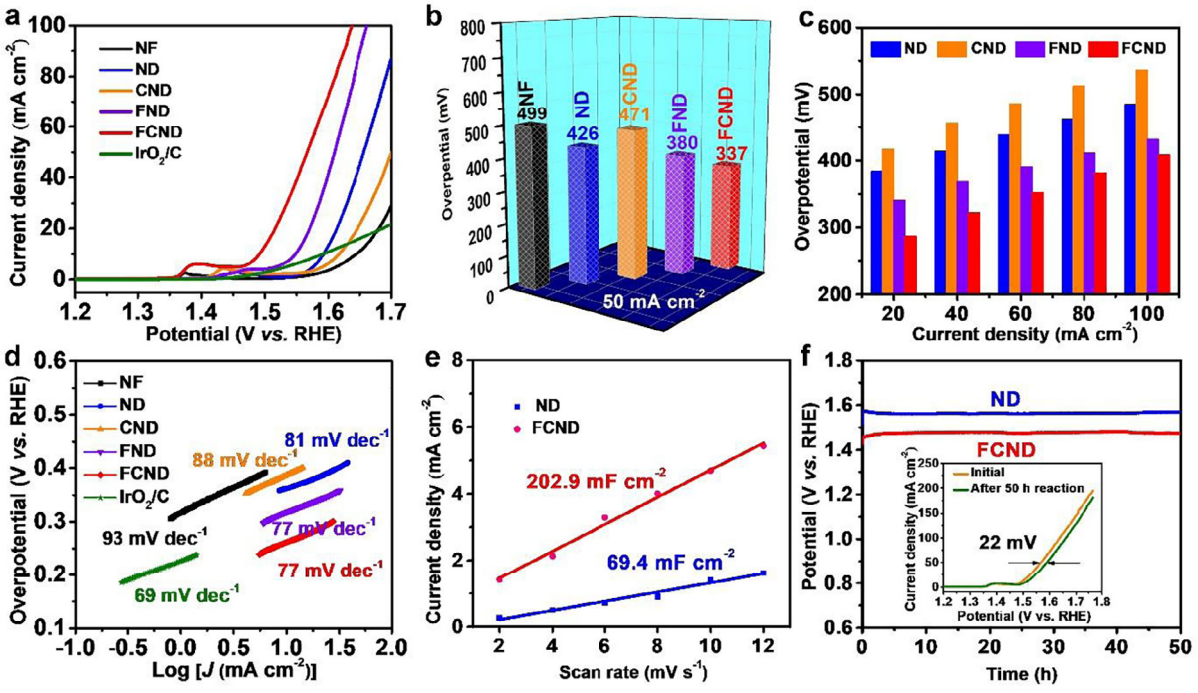

Fig. 3. Polarization curves (a), and overpotential image (b) of NF, ND, CND, FND, FCND, and IrO_2/C. Overpotential image of ND, CND, FND, and FCND at different current densities (c). Tafel plots of NF, ND, CND, FND, FCND and IrO_2/C (d). Current density as a function of scan rate for ND and FCND (e). Chronopotentiometry of FCND at a constant current density of 10 mA cm^{-2} (The inset is a comparison between LSV curves of FCND initial and that after test) (f).

FCND are 69.4 and 202.9 mF cm^{-2}, respectively. The roughness factors of the two electrodes are 1.39×10^4 and 4.06×10^4, respectively. The FCND electrode possesses a high active surface area which is 2.92-fold that of the ND electrode, suggesting the Fe, Co, Ni elements in the ternary transition metal dichalcogenide nanorods on NF produce more active sites exposed. Furthermore, electrochemical impedance spectroscopy (EIS) is further employed to provide more details on the electrochemical performance (Fig. S9). The charge transfer resistance (R_{ct}) of the FCND electrode (0.20 Ω) is similar to that of ND (0.16 Ω), FND (0.15 Ω), and CND (0.17 Ω), excluding the effect of charge transfer capability on the catalytic OER performance. Consequently, the improvement of catalytic performance can be well attributed to the intrinsic activity of the Fe and Co introduction.

In addition to electrocatalytic activity, long-term stability is also an important indicator of OER electrocatalysts. The stable *i-t* curve (Fig. 3f) and overlapped polarization curves are used to evaluate the electrochemical stability of ND and FCND electrodes. After 50 h of the chronopotentiometry test, the potential only increases about 22 mV, demonstrating the excellent stability of the FCND (inset of Fig. 3f). The EIS curve (Fig. S10) and SEM image (Fig. S11) after 50 h of the long-stability test almost remained same as before, which reveals the performance stability of the catalysts. The ND electrode (Figs. 3f, S12, and S13) also shows good stability, which can be ascribed to its special free-standing structure.

2.3. Potential-dependent studies of surface reconstruction in FCND

In order to further study the real active origin in FCND during the OER process, potential-dependent Raman measurements were carried out to monitor the first linear sweep voltammetry (LSV) of the FCND electrode, where the sample recorded at each point in the LSV curve (Fig. 4a) is studied. From the LSV curve, the onset potential is about 1.40 V vs RHE. In the low potential region, the characteristic peaks at around 211, 250, 327, and 372 cm^{-1} in Raman spectra (Fig. 4b) are mainly FCND [46]. When the applied potential increases above 1.5 V, the characteristic peaks of FCND disappears, and the two Raman peaks appear at 484 cm and 558 cm^{-1}, assigns to metal oxyhydroxides. This indicates that the electrode surface has evolved into the oxyhydroxide layer [54]. In the alkaline electrolyte (1.0 M KOH), the Raman peaks for oxyhydroxide are enhanced by further oxidation, suggesting that it is becoming active species, providing M–O bond strength with the formed M–OH, M–O, M–OOH, and M–OO bonds acting as electrocatalytically active intermediates for OER [54,55]. To further investigate the depth of the surface reconstruction, *ex-situ* XRD measurements were used to monitor phase changes after the first LSV and the long-term stability tests. Compared to the initial FCND electrode, the XRD patterns (Fig. 4c) after the first LSV and 24 h long-stability test suggest that the FCND is not completely converted into ternary transition metal oxyhydroxides (FCNOH) phase, rather form an FCNOH covering on the FCND.

To better reveal the surface-interface state after the long-term stability tests (50 h), we conducted studies using HRTEM, HAADF-STEM, STEM-EDS, combined with electron energy loss (EEL) spectra (Fig. 4d–f). As shown in HRTEM (Fig. 4d), there are clear lattice fringes of 0.24 nm that are well-matched to the (0 0 3) planes of FCND in the core. The SAED (inset of Fig. 4d) results also prove that the main phase after the long-term stability test is still FCND. In addition, in the HRTEM image of the surface layer, no obvious lattice fringes were identified, showing the low crystallinity of the FCNOH surface layer. To further confirm the dis-

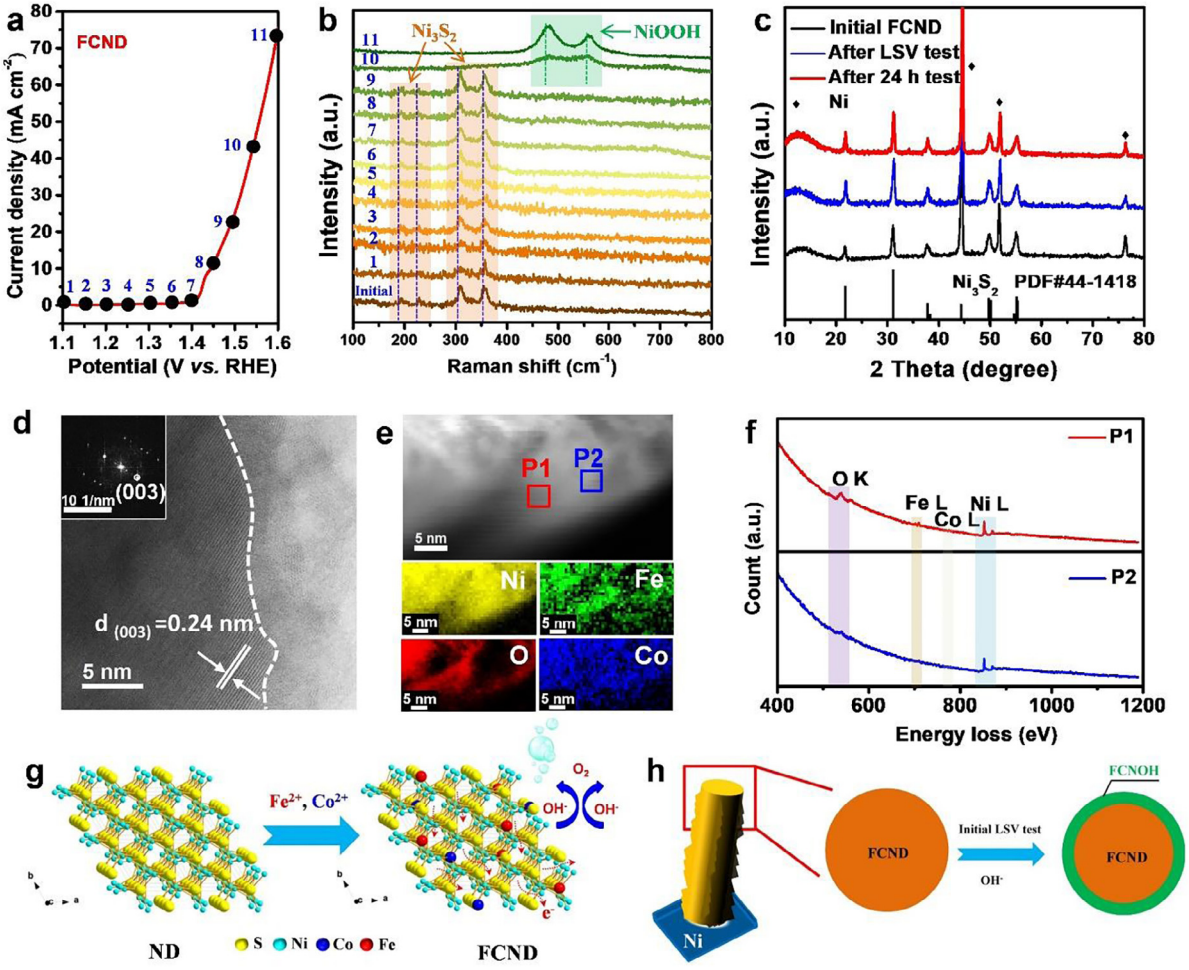

Fig. 4. Recorded first LSV curve (a), and corresponding *in-situ* Raman spectra (b). XRD patterns of FCND after the first LSV and 24 h test (c). HRTEM image (the inserted figure is the corresponding SAED pattern) (d). HAADF-STEM image and EDS mappings of the FCND after 50 h stability test (e). Corresponding EEL spectra were taken at the background in the red and blue boxes in the HAADF-STEM image (f). Schematic diagram of FCND catalytic active site (g). Schematic diagram of the surface reconstruction process (h).

tribution of elements, EDS mappings are collected. As shown in Fig. 4(e), the Ni element is uniformly distributed and has the strongest brightness. Fe and Co are also uniformly distributed and the brightness is much lower than that of Ni, suggesting Fe and Co are present in the surface layer. Interestingly, there is an uneven distribution of O content, indicating that O is largely concentrated in the surface region of the sample. When the electron beam moves to the bright area of oxygen mapping (red box in Fig. 4e), the edges of O K, Fe L, Co L, and Ni L can be detected, thereby confirming that the FCNOH represented by oxygen exists in the FCND (Fig. 4f). In contrast, when the electron beam moves to the dark region of the upper oxygen mapping (blue box in Fig. 4e), the signal of Ni is almost unchanged, but the signal of O becomes almost impossible to detect, and the intensity of Fe and Co signals is greatly reduced. Therefore, it can be concluded that the ultrathin FCNOH shell covers on the surface/subsurface of FCND.

Fig. 4(g) shows the schematic diagram of the pristine FCND catalyst. On the basis of the studies discussed above by combining the morphology and performance analysis, one can conclude: (i) The introduction of Co promotes the nanorod formation, strengthening the structural support; (ii) the introduction of Fe is the main factor leading to the formation of the sheet-like morphology on nanorods and therefore efficiently promotes the internal electron transport and boosts the active surface area. (iii) The surface self-reconstruction into the ultrathin FCNOH shell layer together with the FCND core, as represented by Fig. 4(h), gives rise to the overall chemical and structural entity which is responsible for the high OER performance.

3. Conclusions

In summary, we purposely devised the Fe-Co-Ni ternary transition metal dichalcogenide nanorod arrays (FCND) as a non-precious metal candidate for enhanced OER performance. The resultant FCND nanorod arrays exhibit a lower overpotential and a smaller Tafel slope as well as 27-fold rise in current density at 300 mV overpotential, when compared with the binary and unary counterparts. It also shows an almost unchanged long-term stability upon the test for 50 h in 1.0 M KOH. The FCND nanorods function as a pre-catalyst, which is steadily converted into ultrathin ternary transition metal oxyhydroxides (FCNOH) layer on the surface initiated at ~1.5 V, contributing to the fast OER kinetics and strong stability of the catalysts.

Declaration of Competing Interest

The authors declare that they have no known competing financial interests or personal relationships that could have appeared to influence the work reported in this paper.

Acknowledgments

The authors acknowledge the financial support from the National Natural Science Foundation of China (21673171). J.W. acknowledges the kind support for the academic research by the Ministry of Education Singapore (Tier 1, R284-000-193-114) for research conducted in the National University of Singapore. Q.C. thanks support from the China Scholarship Council (CSC).

Appendix A. Supplementary data

Supplementary data to this article can be found online at https://doi.org/10.1016/j.jechem.2020.07.005.

References

[1] Q. Shi, C. Zhu, D. Du, Y. Lin, Chem. Soc. Rev. 48 (2019) 3181–3192.
[2] D.K.D. Timothy, R. Cook, S.Y. Reece, Y. Surendranath, T.S. Teets, D.G. Nocera, Chem. Rev. 110 (2010) 6474–6502.
[3] G. Chen, Y. Zhu, H.M. Chen, Z. Hu, S.F. Hung, N. Ma, J. Dai, H.J. Lin, C.T. Chen, W. Zhou, Z. Shao, Adv. Mater. 31 (2019) 1900883.
[4] S. Yagi, I. Yamada, H. Tsukasaki, A. Seno, M. Murakami, H. Fujii, H. Chen, N. Umezawa, H. Abe, N. Nishiyama, S. Mori, Nat. Commun. 6 (2015) 8249.
[5] J. Zhang, Z. Zhao, Z. Xia, L. Dai, Nat. Nanotechnol. 10 (2015) 444–452.
[6] T.Y. Ma, J.L. Cao, M. Jaroniec, S.Z. Qiao, Angew Chem. Int. Ed. 55 (2016) 1138–1142.
[7] J.Y. Matthew W. Kanan, Yogesh Surendranath, Mircea Dinca,, D.G.N. Vittal K. Yachandra, J. Am. Chem. Soc. 132 (2010) 13692–13701.
[8] L. Duan, F. Bozoglian, S. Mandal, B. Stewart, T. Privalov, A. Llobet, L. Sun, Nat. Chem. 4 (2012) 418–423.
[9] J.H. Kim, D.H. Youn, K. Kawashima, J. Lin, H. Lim, C.B. Mullins, Appl. Catal. B-Environ. 225 (2018) 1–7.
[10] B.K. Kim, S.-K. Kim, S.K. Cho, J.J. Kim, Appl. Catal. B- Environ. 237 (2018) 409–415.
[11] P. Ding, F. Luo, P. Wang, W. Xia, X. Xu, J. Hu, H. Zeng, J. Mater. Chem. A 8 (2020) 1105–1112.
[12] V. Vij, S. Sultan, A.M. Harzandi, A. Meena, J.N. Tiwari, W.-G. Lee, T. Yoon, K.S. Kim, ACS Catal. 7 (2017) 7196–7225.
[13] Y. Chen, K. Rui, J. Zhu, S.X. Dou, W. Sun, Chem. - Eur. J. 25 (2019) 703–713.
[14] Z. Sun, X. Wang, H. Zhao, S.W. Koh, J. Ge, Y. Zhao, P. Gao, G. Wang, H. Li, Carbon Energy 2 (2020) 122–130.
[15] O. Diaz-Morales, I. Ledezma-Yanez, M.T.M. Koper, F. Calle-Vallejo, ACS Catal. 5 (2015) 5380–5387.
[16] K. Zhu, X. Zhu, W. Yang, Angew Chem. Int. Edit. 58 (2019) 1252–1265.
[17] Q. Chen, R. Wang, M. Yu, Y. Zeng, F. Lu, X. Kuang, X. Lu, Electrochim. Acta 247 (2017) 666–673.
[18] Z. Xue, X. Li, Q. Liu, M. Cai, K. Liu, M. Liu, Z. Ke, X. Liu, G. Li, Adv. Mater. 31 (2019) 1900430.
[19] N.A. Khan, N. Rashid, M. Junaid, M.N. Zafar, M. Faheem, I. Ahmad, ACS Appl. Energy Mater. 2 (2019) 3587–3594.
[20] J. Yin, Y. Li, F. Lv, M. Lu, K. Sun, W. Wang, L. Wang, F. Cheng, Y. Li, P. Xi, S. Guo, Adv. Mater. 29 (2017) 1704681.
[21] X. Ding, W. Li, H. Kuang, M. Qu, M. Cui, C. Zhao, D.C. Qi, F.E. Oropeza, K.H.L. Zhang, Nanoscale 11 (2019) 23217–23225.
[22] Y. Lin, G. Chen, H. Wan, F. Chen, X. Liu, R. Ma, Small 15 (2019) 1900348.
[23] Y. Zhang, J. Fu, H. Zhao, R. Jiang, F. Tian, R. Zhang, Appl. Catal. B- Environ. 257 (2019) 117899.
[24] C. Wang, X. Shao, J. Pan, J. Hu, X. Xu, Appl. Catal. B- Environ. 268 (2020) 118435.
[25] Y. Yang, K. Zhang, H. Lin, X. Li, H.C. Chan, L. Yang, Q. Gao, ACS Catal. 7 (2017) 2357–2366.
[26] Y. Wu, G.-D. Li, Y. Liu, L. Yang, X. Lian, T. Asefa, X. Zou, Adv. Funct. Mater. 26 (2016) 4839–4847.
[27] W. Zhou, X.-J. Wu, X. Cao, X. Huang, C. Tan, J. Tian, H. Liu, J. Wang, H. Zhang, Energy Environ. Sci. 6 (2013) 2921–2924.
[28] T.A. Ho, C. Bae, H. Nam, E. Kim, S.Y. Lee, J.H. Park, H. Shin, ACS Appl. Mater. Interfaces 10 (2018) 12807–12815.
[29] L.L. Feng, G. Yu, Y. Wu, G.D. Li, H. Li, Y. Sun, T. Asefa, W. Chen, X. Zou, J. Am. Chem. Soc. 137 (2015) 14023–14026.
[30] G. Zhang, Y.-S. Feng, W.-T. Lu, D. He, C.-Y. Wang, Y.-K. Li, X.-Y. Wang, F.-F. Cao, ACS Catal. 8 (2018) 5431–5441.
[31] Y. Qu, M. Yang, J. Chai, Z. Tang, M. Shao, C.T. Kwok, M. Yang, Z. Wang, D. Chua, S. Wang, Z. Lu, H. Pan, ACS Appl. Mater. Interfaces 9 (2017) 5959–5967.
[32] N. Cheng, Q. Liu, A.M. Asiri, W. Xing, X. Sun, J. Mater. Chem. A 3 (2015) 23207–23212.
[33] Q. Liu, L. Xie, Z. Liu, G. Du, A.M. Asiri, X. Sun, Chem. Commun. 53 (2017) 12446–12449.
[34] L. Wang, Y. Li, Q. Sun, Q. Qiang, Y. Shen, Y. Ma, Z. Wang, C. Zhao, ChemCatChem 11 (2019) 2011–2016.
[35] Y. Tuo, X. Wang, C. Chen, X. Feng, Z. Liu, Y. Zhou, J. Zhang, Electrochim. Acta 335 (2020) 135682.
[36] R.V. Digraskar, S.M. Mali, S.B. Tayade, A.V. Ghule, B.R. Sathe, Int. J. Hydrogen Energ. 44 (2019) 8144–8155.
[37] Z.W. Seh, J. Kibsgaard, C.F. Dickens, I. Chorkendorff, J.K. Norskov, T.F. Jaramillo, Science 355 (2017) 4998.
[38] M. Yao, N. Wang, W. Hu, S. Komarneni, Appl. Catal. B-Environ. 233 (2018) 226–233.
[39] V.R. Stamenkovic, D. Strmcnik, P.P. Lopes, N.M. Markovic, Nat. Mater. 16 (2016) 57–69.
[40] G. Chen, Z. Hu, Y. Zhu, B. Gu, Y. Zhong, H.J. Lin, C.T. Chen, W. Zhou, Z. Shao, Adv. Mater. 30 (2018) 1804333.
[41] P. Chen, T. Zhou, S. Wang, N. Zhang, Y. Tong, H. Ju, W. Chu, C. Wu, Y. Xie, Angew Chem. Int. Ed. 57 (2018) 15471–15475.
[42] L. Wang, Q. Zhou, Z. Pu, Q. Zhang, X. Mu, H. Jing, S. Liu, C. Chen, S. Mu, Nano Energy 53 (2018) 270–276.
[43] Z. Kou, Y. Yu, X. Liu, X. Gao, L. Zheng, H. Zou, Y. Pang, Z. Wang, Z. Pan, J. He, S.J. Pennycook, J. Wang, ACS Catal. 10 (2020) 4411–4419.
[44] M. Zhou, Q. Weng, X. Zhang, X. Wang, Y. Xue, X. Zeng, Y. Bando, D. Golberg, J. Mater. Chem. A 5 (2017) 4335–4342.

[45] Q. Chen, J. Li, C. Liao, G. Hu, Y. Fu, O.K. Asare, S. Shi, Z. Liu, L. Zhou, L. Mai, J. Mater. Chem. A 6 (2018) 19488–19494.
[46] Z. Cheng, H. Abernathy, M. Liu, J. Phys. Chem. C 111 (2007) 17997–18000.
[47] Q. Chen, J. Jin, Z. Kou, J. Jiang, Y. Fu, Z. Liu, L. Zhou, L. Mai, J. Mater. Chem. A 8 (2020) 13114–13120.
[48] M. Yu, W. Wang, C. Li, T. Zhai, X. Lu, Y. Tong, NPG Asia Mater. 6 (2014) e129.
[49] Y. Zeng, Y. Meng, Z. Lai, X. Zhang, M. Yu, P. Fang, M. Wu, Y. Tong, X. Lu, Adv. Mater. 29 (2017) 1702698.
[50] T. Zhu, L. Zhu, J. Wang, G.W. Ho, J. Mater. Chem. A 4 (2016) 13916–13922.
[51] J.-T. Ren, Z.-Y. Yuan, ACS Sustain. Chem. Eng. 5 (2017) 7203–7210.
[52] C.Z. Yuan, Z.T. Sun, Y.F. Jiang, Z.K. Yang, N. Jiang, Z.W. Zhao, U.Y. Qazi, W.H. Zhang, A.W. Xu, Small 13 (2017) 1604161.
[53] A. Sivanantham, P. Ganesan, S. Shanmugam, Adv. Funct. Mater. 26 (2016) 4661–4672.
[54] S. Klaus, Y. Cai, M.W. Louie, L. Trotochaud, A.T. Bell, J. Phys. Chem. C 119 (2015) 7243–7254.
[55] Y. Jin, S. Huang, X. Yue, H. Du, P.K. Shen, ACS Catal. 8 (2018) 2359–2363.